



Università degli Studi di Messina

**Dipartimento di Scienze biomediche, odontoiatriche e
delle immagini morfologiche e funzionali**

**Dottorato di ricerca in
Bioingegneria applicata alle Scienze mediche (XXXV ciclo)**

Coordinatore Prof. Michele Gaeta

SSD MED/36

**Artificial intelligence in molecular imaging: from
machine to deep learning**

Tutor:

Prof. Sergio Baldari

Co-Tutor:

Prof. Irene A. Burger

PhD Albert Comelli

Dottorando:

Dott. Riccardo Laudicella

Anno Accademico 2021/2022

Index

1. Introduction	1
2. Machine learning experiences	5
2.1 Brain - SPM segmentation, Pyradiomics and machine-learning analysis on [¹⁸ F]FDG brain PET/CT to predict Alzheimer's Disease in patients with positive amyloid PET	5
2.2 Gastrointestinal - Morpho-functional ML radiomics classification of restaging [¹⁸ F]FDG PET/CT for outcome prediction in metastatic colorectal cancer	11
2.3 Neuroendocrine tumor and radioligand therapy - [⁶⁸ Ga]DOTATOC PET/CT ML radiomics to predict the response in GEP-NET undergoing [¹⁷⁷ Lu]DOTATOC RLT: the "theragnostics" concept	16
2.4 Prostate – ML features classification of [¹⁸ F]Choline PET/CT in high-risk prostate cancer outcome prediction	22
3. Deep learning experiences	27
3.1 Brain - Unsupervised Brain Segmentation System Using K-Means and CNN	27
3.2 Prostate - Deep-learning prediction of PSMA PET prostatic volume based on T2 MRI	32
4. Conclusion	36
5. Abbreviations' list	38
6. References	41

1. Introduction

In medical imaging, artificial intelligence (AI) can be described as the system's ability to precisely interpret data, learn from them, and acquire knowledge to achieve specific goals and complete tasks with flexible adaptation. The strength of AI models is the ability to analyze a huge amount of data and generate predictions. Also, in molecular imaging, AI may potentially improve several technical aspects of the daily workflow enabling automatic radiopharmaceutical's synthesis, and improving target delineation/segmentation, images registration, and attenuation correction procedures. Most AI systems are analytical, classified as machine learning (ML) or deep learning (DL) techniques [1-3]. Through a process of "training", these algorithms improve in using and mapping the observed variables ("features" or "predictors") to subdivide the data sample into sets of outcome variables ("labels" or "targets"). Based on "labels", ML can be classified into three broad subsets: supervised, unsupervised, and semi-supervised learning.

1) Supervised learning based on explicit datasets that have been labeled by the operator; in this case, the algorithms measure the difference between the predicted labels and the known labels (called "ground truth"). Linear and logistic regression, support vector machines (SVMs), random forests, and naive bayesian classification belong to this group of ML techniques.

2) Principal component analysis, k-means clustering, and autoencoders instead belong to unsupervised learning. Here, the algorithm optimally separates samples into different classes based on characteristics of the training data alone, without the operator having first defined labels.

3) In semi-supervised (reinforcement) learning, a computer ("agent") learns to perform a task through repeated trial-and-error interactions with a dynamic environment, without being explicitly programmed and without human intervention.

Based on features extraction, ML techniques can be divided into handcrafted (in which the features are explicitly extracted and selected by an operator) and non-handcrafted approaches, in which the process of features extraction and selection is implicitly incorporated into the ML algorithm. ML algorithms can be successfully applied to the vast amount and promising data from radiomics [4]. Using advanced mathematics and statistics, radiomics aims to provide quantitative features that cannot be assessed by human eyes from biomedical images of different natures such as computed tomography (CT), magnetic resonance imaging (MRI), and positron emission tomography (PET). Radiomics assumes that any smallest constituent of each image (i.e., voxel and/or pixel) may encompass features (I order related to the histogram of grey level distribution; II order linked to adjacent pixel/voxel relationship, and so on) of tumor's phenotypes that may be potentially related to tumor's outcome, patients' response to therapy, and so on thus reflecting the pathophysiological process and supporting medical decisions. Radiomics' and machine learning processes can be simply resumed in five main steps as described in **figure 1**: a) acquisition/collection of images b) pre-processing (registration, deconvolution, de-noising, and so on) and volume of interest (VOI) delineation c) feature extraction d) radiomics features reduction and selection of the e) predictive model using AI-based classifiers [1, 2].

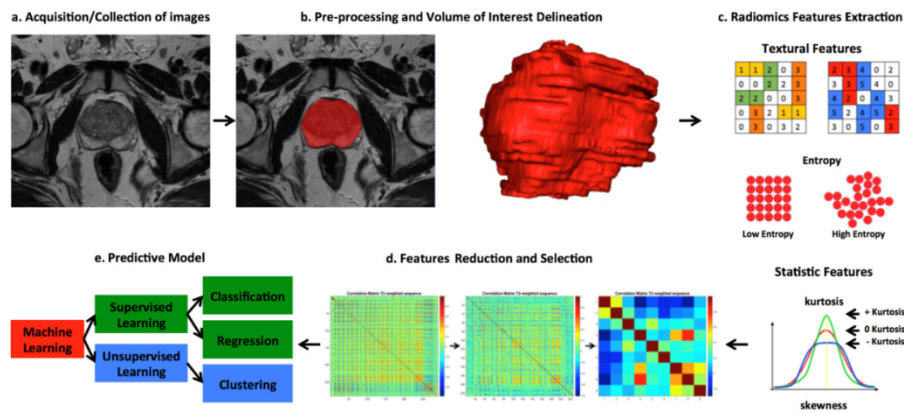


Figure 1. Description of the main machine learning step (from [2]).

ML also encompasses more sophisticated DL techniques that can use both supervised and unsupervised learning. DL methods have a neural network's organization in multiple, progressive, and subsequent related layers (process) reproducing somehow the brain's structure and organization. Each layer analyzes and processes the incoming data (input) from the previous layer, sending it to the next layer until the output is extracted, which usually identifies a classification label or another evaluable property of the dataset [4] thus resulting well suited for huge, diverse, complex data and tasks such as automatic image segmentation and classification (an example in **figure 2**).

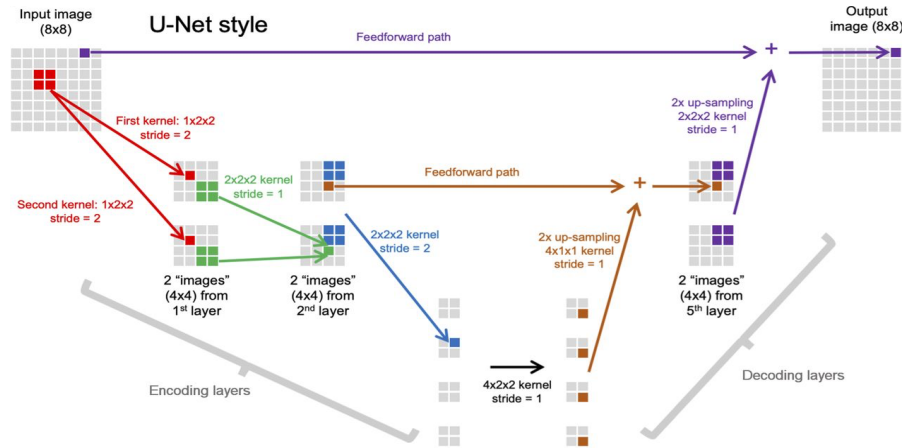


Figure 2. Example of DL U-Net organization in convolutional neural network (CNN) (from [5]).

Despite the great potential of these methods, we must remember that the analysis of grey levels of neighboring voxels in PET depends largely on imaging parameters, especially filters, voxel size, and scatter correction. Strick imaging reconstruction standardization is therefore mandatory, and results need external validation to be meaningful. Also, in real-life, well-annotated large data sets needed for the AI process are often unavailable, and too small datasets are a potential source of error. Furthermore, the harmonization of data from different centers is possible but difficult due to different protocols, equipment, and software.

Before embarking on AI in clinical applications we need to produce, confirm, and reproduce as much data and results as possible following initial guidelines [6, 7].

Accordingly, during my PhD, I learned [1-4, 8, 9] assessed, and applied several aspects, and new potential applications of AI in molecular imaging: from ML image classification [10, 11], prediction of disease outcome [12, 13], prediction of response to therapy [14], to DL segmentation [15]. Finally, during my period at the Universitatsspital of Zurich (USZ) I also accomplished, in collaboration with the Swiss Federal Institute of Technology (ETH), an innovative study (in submission) regarding the prediction of PET volumes from MRI images, assessing simultaneous PET/MRI. In this thesis, I will describe the main results of the abovementioned studies published during my PhD time following an anatomical and computational order.

2. Machine learning experiences

2.1 Brain - SPM segmentation, Pyradiomics and ML analysis on [^{18}F]FDG brain PET/CT to predict Alzheimer's Disease in patients with positive amyloid PET [10]

Background

Alzheimer's disease (AD) is the most common form of progressive and irreversible dementia. Early in-vivo diagnosis of AD is crucial for accurate management of patients, in particular, to select subjects with mild cognitive impairment (MCI) that may evolve into AD [16]. The importance of exploring associated biomarkers for the early diagnosis and prediction of AD progression is a major clinical issue. The National Institute on Aging- Alzheimer's Association (NIA-AA) proposed A/T/N diagnostic criteria in 2018, including A β 42, p-tau, and t-tau in cerebrospinal fluid (CSF), and PET [17]. However, the invasiveness of lumbar puncture for CSF assessment and the limited availability of PET with new radiotracers (for Tau and A β brain burden), represent a valid reason to develop new approaches with AI applied to the more easily available methods such as fluorodeoxyglucose (FDG) PET. In this setting, we proposed a radiomics analysis on FDG PET images based on Statistical Parametric Mapping (SPM) and Pyradiomics, in combination with a ML application, to predict Amyloid-PET positivity and diagnosis of AD.

Methods

From July 2016 to September 2017, 43 patients (median age 64.8 years, Range 53–83 years; females = 23; median Mini-Mental State Examination, MMSE = 19.3, Range 4–28) underwent brain PET/CT scans with FDG and [^{18}F]Florbetaben (FBB), and at least 24 months of clinical/instrumental follow-up (FU). Patients were retrospectively evaluated by a multidisciplinary team (MDT = neurologist, psychologist, radiologist, nuclear medicine physician, and laboratory clinic doctor) at the Fondazione Istituto G.Giglio of Cefalù (Palermo, Italy).

The inclusion criteria were as follows: (a) neurological and neuropsychological suspicion of neurodegenerative disease, based on the NIA-AA and European Federation of Neurological Societies/European Neurological Society (ENS-EFNS) criteria [18]; (b) MRI brain imaging to rule out moderate or severe cerebrovascular defects; (c) FDG PET/CT performed for metabolic assessment; (d) availability of an FBB PET/CT within 6 months from conventional imaging and FDG PET/CT scan; (e) report of the positivity/negativity of FBB-PET and MDT meeting with the final diagnosis for each patient; (f) minimum duration of neurological and neuropsychological FU of 24 months after the first neurological evaluation for the cognitive defect, used to estimate the disease status, to allow the assessment of disease progression over time, and confirm/exclude the in-vivo diagnosis of AD.

Image Pre-Processing and ROI Selection

The whole dataset was spatially pre-processed using SPM 12 software package (<https://www.fil.ion.ucl.ac.uk/spm/>). First, each FDG PET scan, comprising 47 Digital Imaging and Communications in Medicine (DICOM) images, was converted into a single NIfTI file, preserving the original spatial resolution. Then, the resulting 3D volume was spatially normalized to the Montreal Neurological Institute (MNI) 152 space, using the SPM unified segmentation normalization algorithm, which combines segmentation, bias correction and spatial normalization in a single process of optimization. This iterative method, which provides better results than simple serial applications of each step, allowed us to directly estimate the warping tensors that register the SPM standard spatial priors (i.e., tissue probability maps) in each individual subject space. The intensity distribution of each class of tissue has been modelled by at least a mixture of two Gaussians to consider the partial volume effect; furthermore, a smoothness level of 5 mm was set to derive a fudge factor related to the spatial correlation between neighbouring voxels, due to the assumption of independence of the unified model [19]. The default settings were used for all other parameters. Then, the estimated nonlinear spatial transformations were applied and the PET images were resampled in a bounding box with an isotropic voxel size of 2 mm, reflecting the MNI-152 spatial proportions

in a similar way to previous works [20]. After spatial normalization, we focused on four different regions of interest (ROIs) that were extracted from the brain fragmentation available in SPM, whose maximum probability tissue labels derived from the “MICCAI 2012 Grand Challenge and Workshop on Multi-Atlas Labelling” (<https://my.vanderbilt.edu/masi/workshops>). This neuro-anatomical classification was generated and made public by Neuromorphometrics, Inc. under an academic subscription and provides a precise subdivision of cortical and non-cortical structures, for a total of 138 labels throughout the brain. Each selected ROI included 8 to 12 brain areas labelled according to **table 1**, and, prior to mask extraction, their bounding box and voxel sizes were adapted to the template for alignment reasons.

ROI 1	Areas	Label Index	ROI 2	Areas	Label Index	ROI 3	Areas	Label Index	ROI 4	Areas	Label Index
	Right Hippocampus	47		Right (AOrG anterior orbital gyrus	104		Right FuG fusiform gyrus	122		Right PO parietal operculum	174
	Right PHG parahippocampal gyrus	170		Right MOrG medial orbital gyrus	146		Right GRe gyrus rectus	124		Right PoG postcentral gyrus	176
	Right Ent entorhinal area	116		Right OpIFGopercular part of the inferior frontal gyrus	162		Right ITG inferior temporal gyrus	132		Right SPL superior parietal lobule	198
	Right MTG middle temporal gyrus	154		Right OrIFG orbital part of the inferior frontal gyrus	164		Right TMP temporal pole	202		Right PCgG posterior cingulate gyrus	166
	Left Hippocampus	48		Right MFC medial frontal cortex	140		Left FuG fusiform gyrus	123		Right PCuprecuneus	168
	Left PHG parahippocampal gyrus	171		Right MFG middle frontal gyrus	142		Left GRe gyrus rectus	125		Left PoG postcentral gyrus	177
	Left Ent entorhinal area	117		Left MOrG medial orbital gyrus	147		Left ITG inferior temporal gyrus	133		Left PO parietal operculum	175
	Left MTG middle temporal gyrus	155		Left AOrG anterior orbital gyrus	105		Left TMP temporal pole	203		Left SPL superior parietal lobule	199
				Left OpIFGopercular part of the inferior frontal gyrus	163					Left PCuprecuneus	169
				Left OrIFG orbital part of the inferior frontal gyrus	165					Left PCgG posterior cingulate gyrus	167
				Left MFC medial frontal cortex	141						
				Left MFG middle frontal gyrus	143						

Table 1. ROI extracted from the cerebral segmentation using SPM (from [10]).

Extraction of radiomics features and ML classification

The ROIs described in **table 1** were used to extract the FDG PET features through a certified and image biomarker standardisation initiative (IBSI) [20] compliant software, namely Pyradiomics [21]. Subsequently, an innovative descriptive-inferential mixed sequential approach for feature reduction and selection was used to identify a small set of radiomics features with a strong association with patient outcomes to obtain good predictive

performance, leading to the exclusion of non-reproducible, redundant and irrelevant features from the initial set [22]. Indeed, for each feature, the point biserial correlation (pbc) index between features and the dichotomic outcome (AD versus non-AD) was calculated, sorting the features in pbc descending order. Then, a cycle started to add one column at a time, performing a logistic regression analysis by comparing the p -value of each iteration and stopping in the case of a growing p -value. After this selection and reduction process, discriminant analysis (DA) was used as the predictive model [23]. The training phase was performed only once and, after being completed, the DA was able to classify new cases. Using the k-fold cross-validation strategy, the data was split into training and validation sets using a random partition. Specifically, the data were divided into k-folds: one of the folds was used as a validation set and the remaining folds were combined into the training set. The pooling was done so that both the training and validation sets maintained the same positive/negative percentage for beta-amyloid deposition compared to the original dataset. Then, the average error across all experiments was computed. In this way, (i) overfitting and asymmetrical sampling are avoided, thus increasing the accuracy of results; (ii) several models can be tested; (iii) the results averaged over all the folds are more robust. In our study, $k = 5$ was determined empirically by the trial-and-error method (range k : 5–15, a step of 5). Based on the above systems we defined the FDG features able to reach the best diagnostic performance in predicting amyloid deposition and the final diagnosis of AD.

Performance evaluation

The diagnostic performance was calculated including sensitivity, specificity, and accuracy. The sensitivity is the number of correctly classified positive samples divided by the number of true-positive (TP). The specificity is the number of correctly classified negative samples divided by the number of true-negative (TN) samples. The accuracy is defined as $(TP + TN) / (TP + FP + FN + TN) \times 100$, where FP is the number of false-positive, and FN is the number of false-negative. In addition, receiver operating characteristics (ROC) with 95% confidence interval (CI) and areas under the ROC curve (AUC ROC; 95% CI) were calculated to assess

the performance of the predictive models (DA) obtained considering (a) the individual features identified using the reduction and selection process, and (b) the combination of the same individual features.

Results

Following the MDT evaluation, based on the results of the neuropsychological tests, the dosage of the levels of specific proteins (amyloid and tau) in the CSF (if available), integration/comparison with MRI, and evaluation of the evolution of the disease until last neurological evaluation (> 24 months), 22/23 amyloid-PET positive patients were definitively classified as AD patients, while the remainder as non-AD.

Radiomics' features analysis

As regards the performance in the prediction of the final clinical-instrumental diagnosis of AD defined by MDT evaluating all the available data, we obtained the best results considering the following higher-order feature from the second ROI (including the anterior and medial orbital gyri of the inferior frontal cortex and the medial frontal cortex, **figure 3**): `original_glm_MCC` and `original_glm_MaximumProbability` with a sensitivity of 75.2%, specificity of 80.5%, and accuracy of 78.05% ($p = 0.002$).

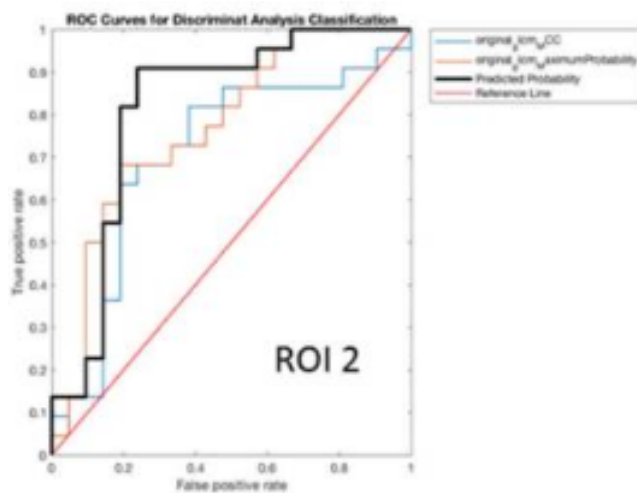


Figure 3. AUC ROC of FDG-PET higher order features `original_glm_MCC` and `original_glm_MaximumProbability` in the prediction of AD (from [10]).

Discussion

The first objective of our study concerned the application of AI on FDG PET/CT brain images in predicting PET-Amyloid positivity, eventually avoiding the additional execution of an amyloid-PET as a diagnostic method not widely diffuse compared to FDG-PET/CT, ultimately reducing the social and economic impact on the health system. Secondly, the opportunity to select those patients who can benefit from the diagnostic use of amyloid-PET and to evaluate how the integration of the functional and pathophysiological information of the two investigations can improve the diagnostic accuracy for AD through the help of AI. In our analysis for the prediction of AD, the best values were obtained for two higher-order features (original_glm_MCC and original_glm_MaximumProbability). The regions from which these features were extracted concerned the ROI 2, including the anterior and medial orbital gyri of the inferior frontal cortex and the medial frontal cortex. The population studied was characterized by a median age of 64.8 years and a median MMSE value of 19.27, thus configuring a good number of patients with MCI and early onset supporting the possible metabolic involvement of the frontotemporal synaptic connections in early-onset AD (EOAD) forms. Some authors in the literature assessed the risk factors more associated with the conversion from MCI to AD [24], also through radiomics [25, 26] and DL [27] reaching similar or slightly superior results than our model. However, none of them assessed the amyloid-PET information integrating these data to create a reference standard for predicting the diagnosis of AD. Despite limitations (heterogeneous population, uneasy reproducibility in clinical practice), this new automated learning approach based on the extraction and selection of higher-order radiomics “features” obtained from FDG PET/CT brain images resulted promising for predicting the presence of beta-amyloid deposition and the final diagnosis of AD. Such data sustain the potential role of specific radiomics FDG PET features to improve the prognostic stratification of patients who could obtain real diagnostic benefits from amyloid-PET.

2.2 Gastrointestinal - Morpho-functional ML radiomics classification of restaging [^{18}F]FDG PET/CT for outcome prediction in metastatic colorectal cancer [11]

Background

Colorectal cancer (CRC) is the third most common cancer and the second leading cause of death worldwide. Almost 20% of such patients will develop metastatic disease, with about one-third of patients already presenting liver metastases at the time of diagnosis [28]. Alongside traditional imaging (e.g., ultrasonography, CT, MRI), [^{18}F]FDG PET/CT is routinely used as a tool for accurate staging and restaging after therapy in metastatic CRC, and it represents a valuable ally for risk assessment, prognosis evaluation, and treatment strategy decisions making. The further integration of [^{18}F]FDG PET/CT data with radiomics features could reach new insightful information also regarding tumor biology. Radiomics' literature in CRC is highly limited in PET imaging, but nonetheless, it holds promise for genetic mutation status assessment [29] and the prediction of outcomes. The present experience aimed to investigate the potential application of texture analysis on restaging [^{18}F]FDG PET/CT images in metastatic CRC, proposing a radiomics model able to select PET and CT imaging features for global disease status prediction.

Methods

Between November 2008 and December 2018, 63 metastatic lesions from 52 CRC patients were retrospectively considered following these inclusion criteria: (a) pathology confirmed diagnosis of primary colorectal adenocarcinoma; (b) clinical-instrumental (contrast enhancement CT – ceCT -, MRI, histopathology, and/or clinical report) confirmed metastatic disease status; (c) [^{18}F]FDG PET/CT performed at Fondazione Istituto G.Giglio of Cefalù (Palermo, Italy) for restaging after first adjuvant therapy (1 patient treated by radiotherapy – RT -, 49 patients by chemotherapy, and 2 patients by both); (d) [^{18}F]FDG PET/CT positive for lymph-nodal/metastatic disease; (e) minimum FU duration of 12 months after [^{18}F]FDG

PET/CT; (f) complete clinical (clinical case notes and multidisciplinary meeting reports), laboratory, pathological and imaging data available (ceCT, MRI); (g) [^{18}F]FDG PET/CT findings retrospectively confirmed at clinical FU with biopsy and/or through other imaging modalities. The study was approved by the institutional review board. The internal procedures provided informed consent also regarding the potential scientific use of all nuclear medicine examinations. Therefore, written informed consent was available for each patient.

Radiomics analysis

Two board-certified nuclear medicine physicians evaluated and segmented FDG PET/CT lesions by consensus and were blinded to the purpose of the study and to the pathology information. Signal intensity on PET images was judged as hyperintense when the signal intensity of the tumor was higher than the signal intensity of non-tumoral tissue. Maximum standardized uptake value SUV_{max} was used as a PET parameter to select the most avid lesion for the global evaluation of disease status and for the most avid liver lesion in every patient. The same volume was transposed in the same region on CT images for extraction of morphological features. Successively, 105 and 66 features were automatically extracted using the IBSI-compliant software LifeX [30] from each lesion VOI in PET and CT images, respectively. Successively, the mixed descriptive-inferential sequential approach followed by DA with k-fold validation (already described in [22, 23], page 7, **figure 4**), were used to identify a small set of radiomics features (only from PET and then from PET and CT) with valuable association with patients' outcomes for better predictive performance, leading to the exclusion of non-reproducible, redundant, and non-relevant features from the initial features dataset.

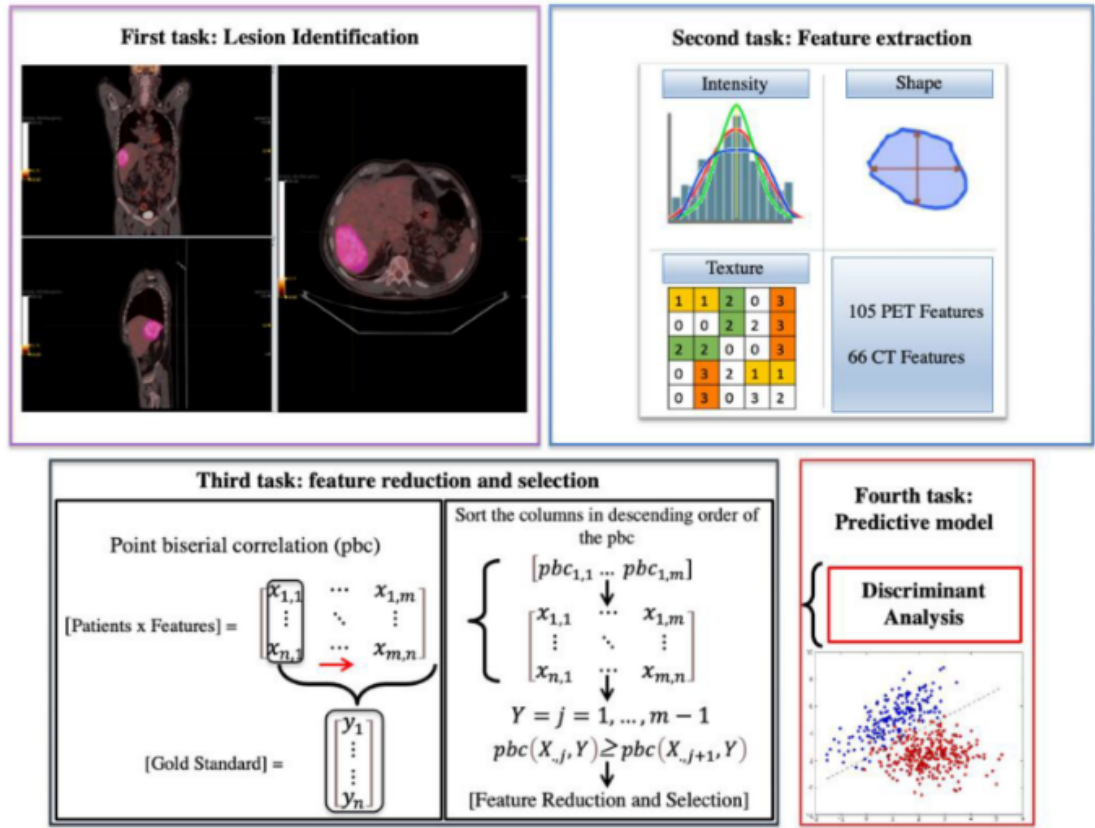


Figure 4. Description of the main machine learning steps (from [11]).

Results

At the first [^{18}F]FDG PET/CT scan, 43 patients (82.7%) were PET-positive for a single lesion and 9 (17.3%) for 2 or more lesions. Sites of metastasis were distributed as follows: 23 liver (36.5%), 12 lymph nodes (19%), 8 lungs (12.7%), 7 presacral lymph nodes (11.1%), 4 peritoneum (6.3%), 3 rectum (4.8%), 2 spleen (3.2%), 2 bones (3.2%), 1 thorax (1.6%), and 1 anastomotic tissue (1.6). At the last FU, 32 (62%) patients showed progression of the disease, 9 (17%) stable disease, and 11 (21%) responded to therapy with a regression of the disease.

At lesion level analysis, GLRLM-based feature grey-level non-uniformity (GLZLM_GLNU) was selected considering the only PET data set obtaining a sensitivity of 90.1%, specificity of 36.8%, accuracy 66.7%, and AUC ROC of 56.5%; the addition of two CT features (GLZLM_ZLNU, and GLRLM_Short Run High Gray-Level

Emphasis—GLRLM_SRHGE) reached the following results (PET/CT): sensitivity 78.2%, specificity 51.75%, accuracy 66.6%, and AUC ROC 65.2% (**figure 5**).

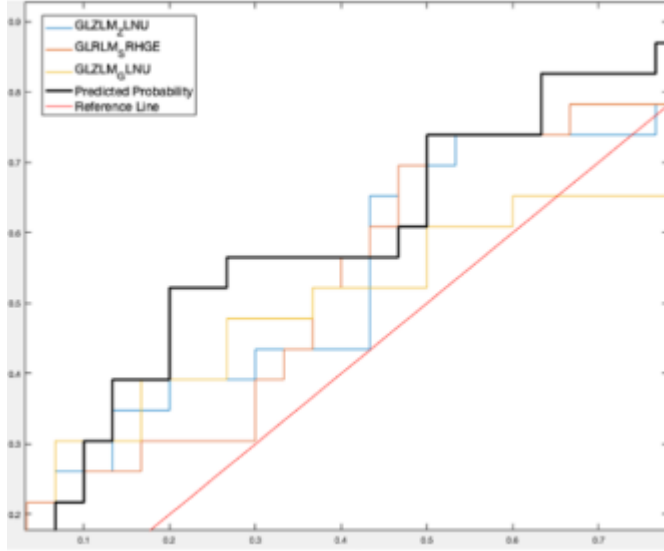


Figure 5. AUC ROC of FDG-PET/CT features in the prediction of patients' outcome (from [11]).

Discussion

Prediction of outcome in patients with CRC is challenging because of the lack of a robust biomarker and heterogeneity between and within tumors to modulate treatment strategies. In this scenario, a study conducted on third-line treatment patients with metastatic CRC showed that high tumor heterogeneity, volume, and low sphericity on baseline [^{18}F]FDG PET were related to reduced survival [31]. Similarly, textural parameters as the coefficient of variation, kurtosis of the absolute gradient (GrKurtosis), and other features on [^{18}F]FDG PET images have been proposed in other papers as predictive and prognostic factors in the assessment of therapy response and survival outcomes in patients with rectal cancer [32]. Differently from other studies in the literature, we demonstrated the potential predictive value of FDG PET/CT radiomics features using an innovative ML model considering the disease status at follow-up as the gold standard for the performance analysis. Namely, in the per-lesion analysis, the most accurate FDG PET feature was GLZLM_GLNU that with the addition of 2 low-dose CT

features (GLZLM_ZLNU and GLRLM_SRHGE) reached an AUC ROC of 65.2%. The apparent sub-optimal results obtained in the present study need to be interpreted with caution because we are not presenting the performance on the identification of disease but the ability of some radiomics features to predict the disease status outcome of metastatic CRC after the standard first adjuvant therapy.

Among limitations, this is a retrospective single-center study, with a relatively small number of patients. All patients who underwent [^{18}F]FDG PET/CT after the first adjuvant therapy were at different disease stages, treated with different chemotherapy combinations following Italian oncological guidelines (5FU or oral capecitabine in combination with either oxaliplatin or irinotecan in various schedules) and a different number of cycles based on patients clinical conditions. All these variables might affect the patient's outcome. In addition, radiomics features were extracted only according to the [^{18}F]FDG-positive tumor to construct the model, and the remaining normal tissue in the image may still contain invisible but useful data. To properly analyze the entire images, 3D DL methods will be necessary. Nevertheless, our preliminary ML model on restaging [^{18}F]FDG PET/CT demonstrated to be feasible and potentially useful in the predictive evaluation of disease progression in metastatic CRC after third-line therapies. This experience suggests that PET texture analysis is feasible and could be used as an independent indicator for the prognosis of patients with a high risk of disease progression, thus supporting clinicians for a more accurate selection of patients that may benefit from tailored therapies.

2.3 Neuroendocrine tumor and radioligand therapy - [^{68}Ga]DOTATOC PET/CT ML radiomics to predict the response in GEP-NET undergoing [^{177}Lu]DOTATOC radioligand therapy: the “theragnostics” concept [14]

Background

Neuroendocrine tumors (NETs) are heterogeneous and rare neoplasms, even if their incidence rate has increased consistently during the last decades, mainly represented by the gastroenteropancreatic (GEP) subtype (up to 70% of all NET). Targeted somatostatin receptor 2 (SSTR 2) molecular imaging with PET/CT or PET/MRI plays a significant role in this scenario, especially for therapeutic decisions including radioligand therapy (RLT) which is an effective treatment for metastatic/inoperable NET, recently approved in Europe, USA, and Canada for GEP forms [33]. RLT represents an application of theragnostics enabling, through a unique radiopharmaceutical administration for multiple cycles, a molecularly targeted therapeutic procedure (i.e., beta minus emission of ^{177}Lu) and biodistribution imaging (i.e., gamma emission of ^{177}Lu). Although it is effective in most cases, approximately 15–30% of GEP NET patients will progress during RLT and can benefit from timely adjustments, therapy combinations, rapid sequencing, or alternatives. Furthermore, a Delphic consensus for GEP NET response to therapy assessment defined both the RECIST 1.1 criteria, PET parameters, and conventional biomarkers as suboptimal due to the high variability in SSTR expression, the different histological patterns related to disease heterogeneity, heterogeneous responses, and lack of standardized criteria for molecular imaging [34]. Therefore, the identification of new and reliable quantitative imaging parameters could be crucial to better address eligible candidates and assess the response to RLT, early selecting the best therapeutic opportunity, avoiding high-costly treatments and related toxicities [35]. Indeed, we aimed to develop a radiomics (“radiOMICS”) predictive model of response analyzing [^{68}Ga]DOTATOC PET/CT images before and after complete [^{177}Lu]DOTATOC RLT (“THERAGNOstics”) in well-

differentiated, progressive, metastatic GEP NET, namely “Theragnostics” that can be applied in a clinical decision support system (CDSS).

Methods

In this retrospective study, we included all consecutive well-differentiated GEP NET patients who, between 1 April 2013 and 30 November 2019, underwent a baseline [^{68}Ga]DOTATOC PET/CT within 2 months before beginning the RLT with [^{177}Lu]DOTATOC performed at the nuclear medicine department of Policlinico G. Martino (University of Messina), and a FU [^{68}Ga]DOTATOC PET/CT available within 9 months after the last RLT cycle. Chromogranin A (CgA) was also assessed before each RLT cycle and at the end of the treatment. Clinical, laboratory, and [^{68}Ga]DOTATOC PET/CT FU data were collected for a period of at least 3 months after the last cycle. In **figure 6** we described the study workflow.

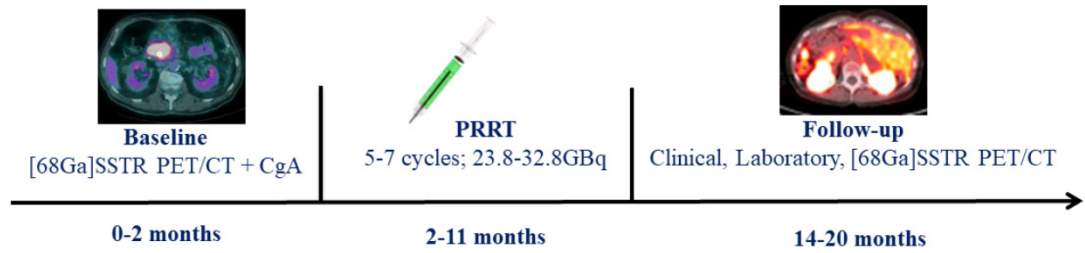


Figure 6. Study workflow (from [14]).

The study was approved by the institutional review board (668-18/20), conducted according to the Declaration of Helsinki principles and good clinical practice guidelines, and written informed consent specifying the potential use of anonymized data for research purposes was obtained for each patient.

For each patient, all [^{68}Ga]DOTATOC-positive lesions that were clearly discriminated, and non-confluent were selected. PET images were imported to LifeX [30] and a 2D-circular ROI was drawn around every lesion. ROIs had a minimum size of 0.443 cm^3 (corresponding to at least 16 voxels) to allow for a consistent textural feature calculation. ROI size was adjusted to the size of the lesions, without incorporating adjacent tissue. In this way, using an absolute

intensity rescaling factor of 0–60 of the SUV (64 bins, 0.95 fixed bin width), 65 radiomics features were automatically extracted for each lesion. In addition, five clinical features were also considered: grading (G1-G2-G3), number of RLT cycles, RLT cumulative activity, pre- and post-RLT CgA values. Therefore, all the features (imaging and clinical) were correlated with the response data through the mixed descriptive-inferential sequential approach followed by DA with k-fold validation (already described in [22, 23], page 7, **figure 7**). Accordingly, the features with valuable association with the outcome were identified and assessed (singularly and in combination) for response to RLT prediction.

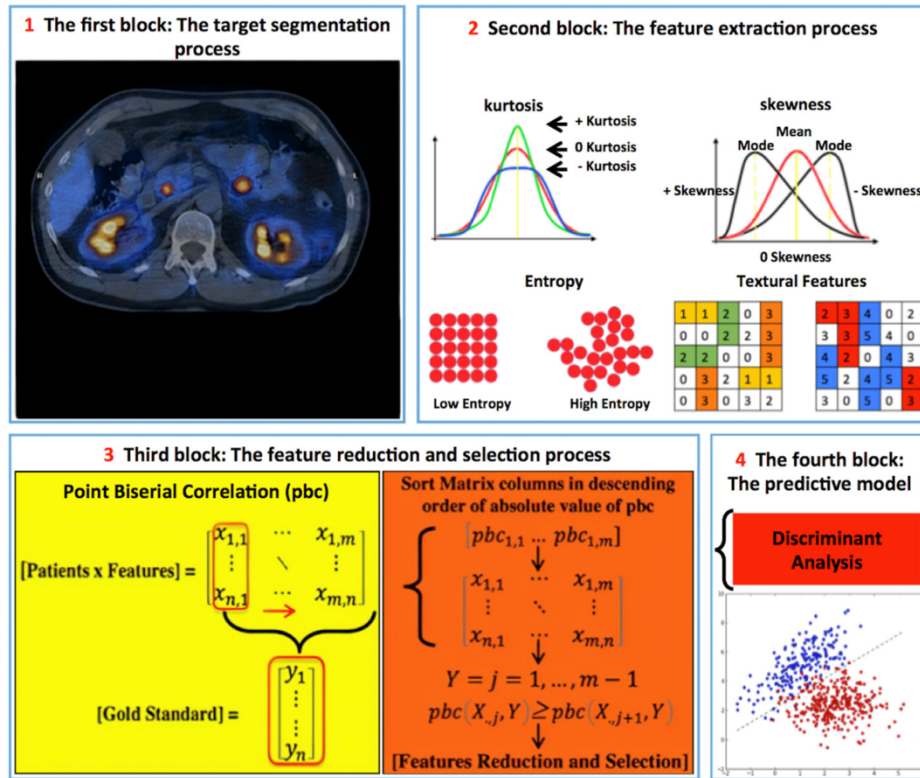


Figure 7. Description of the main machine learning step (from [14]).

For the most significant features, we also assessed the percentage difference value before (T0) and after RLT (T1) in terms of delta radiomics, translating the pre-RLT [^{68}Ga]DOTA-peptide PET/CT ROI in the same lesion area of the follow-up performed within nine months after RLT. The delta radiomics was then calculated using the following formula:

$$\Delta = 100 * (\text{Feature T1} - \text{Feature T0}) / \text{Feature T0}$$

Results

A total of 38 well-differentiated GEP NET patients with a median age of 58 years (range 35–79, 15/38 female) were retrospectively included and underwent a baseline [⁶⁸Ga]DOTATOC PET/CT (median 120.5 MBq, range 93–330) a mean of 1.4 ± 0.7 months before complete RLT with a median cumulative dose of 29 GBq (23.9–32.8), followed by [⁶⁸Ga]DOTATOC PET/CT (median 128.5 MBq, range 93–330) a mean of 8.7 ± 1.1 months after the last RLT cycle. The primary sites originated from the pancreas in 17 out of 38, ileum 14 out of 38, colon three out of 38, stomach two out of 38, and jejunum two out of 38. Grading was distributed as follows: 9/38 G1, 27/38 G2, 2/38 G3. [¹⁷⁷Lu]DOTATOC RLT was performed with a median of five cycles (5–7). Baseline median CgA was 277 ng/mL (17–1315), while follow-up CgA was 125.5 ng/mL (16–1630). At baseline [⁶⁸Ga]DOTATOC PET/CT, we obtained 324 SSTR-positive lesions with at least 16 voxels. Based on their location, lesions were divided as follows: 169 in 324 liver, 91 in 324 lymph nodal, 42 in 324 bone lesions, and 22 in 324 parenchymal (different than liver). At the qualitative assessment of FU [⁶⁸Ga]DOTATOC PET/CT, 133 in 324 lesions were classified as progressive disease (PD) and 191 lesions as responsive to therapy (stable disease – SD -, partial response – PR -, and complete response - CR). The best result for prediction of response to RLT was obtained for HISTO_Skewness with an optimal cut-off at 2.45 reaching an AUC ROC, sensitivity, and specificity of 0.745, 80.6%, and 67.2%, respectively. Differently, the conventional parameter SUV_{max} was not significant ($p = 0.49$, AUC ROC 0.523, sensitivity 36.7%, specificity 63.3%) as shown in **figure 8**.

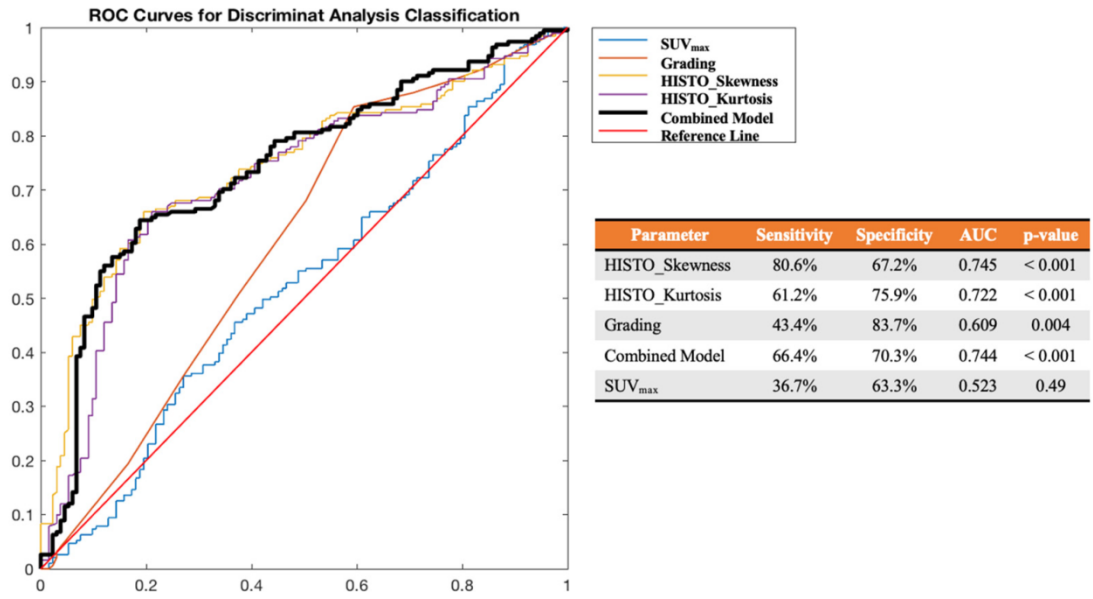


Figure 8. ROC curve analysis for significant features (alone and in combination with clinical variables) and SUV_{max} in the prediction of response to RLT (early FU status) in terms of PD vs. positive results (SD, PR, CR) (from [14]).

Furthermore, HISTO_Skewness was significantly higher ($p < 0.001$) in non-responders than in responders' lesions before and after RLT. Indeed, we also assessed the delta skewness observing in RLT responsive lesions a mean percentage reduction for Δ HISTO_Skewness ($-3.31\% \pm 664.3\%$); differently, for PD, we observed a mean percentage increase for Δ HISTO_Skewness ($112.54\% \pm 348.3\%$; $p = 0.209$).

Discussion

In our preliminary experience, we aimed to give weight to a predictive model of response to RLT based on the most significant [^{68}Ga]DOTATOC PET/CT features. In the innovative but uncertain setup of radiomics applied to GEP-NET, we tried to reproduce a real-life scenario: well-differentiated GEP-NET who underwent [^{68}Ga]DOTATOC PET/CT with different scanners before and after complete RLT. In this way, the feature "HISTO_Skewness" was able to predict the RLT response on lesion-based regardless of the origin/nature with an AUC ROC of 0.745 (cut-off 2.45), sensitivity of 80.6%, and specificity of 67.2%. Also, at Δ radiomics analysis, we observed different lesions' behaviour according to the presence of response,

observing in responsive RLT lesions a mean percentage reduction of the “asymmetry” (namely, Skewness) than non-responsive lesions. A few studies already assessed the potential application of ML in GEP-NET to predict response to RLT. However, such studies referred to very limited and heterogeneous cohorts, or considered only predefined features [36, 37]. Recently, Önner et al. assessed the value of two predefined first-order features, “skewness” and “kurtosis” (interestingly the same as our study, that we obtained in a non-predefined way), in the prediction of response to RLT in 22 GEP NET patients for a total of 326 lesions reaching, however, less significant results (AUC ROC of 0.619 for skewness vs. 0.745 in our paper) [37].

Despite limitations (2D approach, missing external validation), the presented preliminary “theragnomics” model proved to be superior to conventional quantitative parameters to predict the response of GEP-NET lesions in patients treated with complete [¹⁷⁷Lu]DOTATOC RLT, regardless of the lesion site. The opportunity to assess for each patient the single lesion’s heterogeneity and predict each lesion’s response to RLT would enhance physicians to early address patients to the best options of care, reducing costs and potential toxicities, improving quality of life and survival.

2.4 Prostate – ML features classification of [¹⁸F]Choline PET/CT in high-risk prostate cancer outcome prediction [12, 13]

Background

Despite the high success rates of primary definitive therapeutic options, the mortality rates of prostate cancer (PCa) remain high with about 20–50% of patients who experienced biochemical recurrence (BCR) during the FU [38]. In this regard, radiomics analysis of tumors may be useful also for outcomes evaluation by using statistical, shape-based, and/or textural features analysis, including first-, second-, and higher-order methods of increasing complexity. A few numbers of studies reported a correlation between PCa outcome and ¹¹C/¹⁸F-Cho PET/CT–derived semiquantitative parameters: recently, our group suggests in a preliminary report the additional and potential value of PET-derived radiomics features using a ML extraction approach in a sample of patients with high-risk PCa [12]. However, the use of PET image features extracted through AI in the evaluation of high-risk PCa patients has not yet been confirmed in an adequate sample size obtained considering fewer features than samples to avoid the “Large P (P = dimension of independent variables), small N (N = sample size)” problem, i.e., the number of features is much larger than the sample sizes [39]. Indeed, the aim of this study was to investigate the potential application of texture analysis on restaging [¹⁸F]Cho-PET/CT images and to propose a model incorporating a new ML radiomics model to select those features able to predict the disease progression in BCR PCa.

Methods

We retrospectively analyzed ninety-four high-risk PCa patients among 425 patients referred to the nuclear medicine department of Fondazione Istituto G.Giglio of Cefalù (Palermo, Italy) who underwent restaging [¹⁸F]Cho-PET/CT after first-line therapy between November 2013 and May 2018. Inclusion criteria were as follows: (a) pathology confirmed diagnosis of primary high-risk PCa; (b) [¹⁸F]Cho-PET/CT performed at restaging for BCR PCa after

primary therapy resulted positive for local recurrence or lymph-nodal/metastatic disease; (c) minimum FU of 12 months (mean 22 months) after [¹⁸F]Cho-PET/CT including complete clinical (clinical case notes and multidisciplinary meeting reports), laboratory, pathological, and imaging data available (ceCT, MR, and bone scan – BS); (d) [¹⁸F]Cho-PET/CT findings retrospectively confirmed at clinical FU and/or by means of other imaging modalities. Based on such information, the disease status during the FU was defined as PD or SD. The study has been approved by the institutional review board. The internal procedures provide informed consent also regarding the potential scientific use of all nuclear medicine examinations performed at our institution. Therefore, written informed consent was available for each patient.

Radiomics features extraction and machine-learning features classification

For ROI selection, a semi-automatic and operator-independent segmentation system was used [40]. Accordingly, the user intervention is limited to drawing an initial contour around the tumor. Starting from this contour, all the following steps are automatically performed to identify an optimal, operator-independent, initial ROI around the tumor. This process is based on the SUV_{max} voxel that is used as a target speed for the region growing segmentation to obtain a rough estimate of the lesion boundary. This initial operator-independent ROI is the input to the next component of the system, an enhanced local active contour segmentation algorithm, as extensively reported in [40]. Accordingly, the proposed system identifies user-independent volumetric segmentation. These segmentations are then imported into LIFEx toolbox [30] to extract features from each lesion by defining subgroups as follows: a) Primary tumor or local relapse (T); b) Lymph-nodal disease (N); c) Bone metastasis (M); d) Whole sample. Also, prostate-specific antigen (PSA) and Gleason score features were considered ($51 + 2 = 53$ features). Successively, the mixed descriptive-inferential sequential approach followed by DA with k-fold validation (already described in [22, 23], page 7, **figures 4 and 7**), were used to identify a small set of radiomics features with valuable association with

patients' outcomes for better predictive performance, leading to the exclusion of non-reproducible, redundant, and non-relevant features from the initial feature data set.

Results

Ninety-four patients (mean age 75 years) with a mean PSA value of 74.2 ng/mL scanned between November 2013 and May 2018 met the inclusion criteria. As a first-line treatment, 15 patients (16%) underwent radical prostatectomy (RPE) and pelvic lymph-nodal dissection, 22 patients (23%) were treated with RPE followed by pelvic-prostate RT, 11 patients (12%) underwent RPE followed by hormone therapy, 14 patients (15%) with pelvic-prostate RT followed hormone therapy, 26 patients (28%) were treated only with hormone therapy, and 6 patients (6%) with hormone therapy and zoledronate. At the qualitative assessment, 7/94 (7%) patients were PET-positive for T, N, and M; 10/94 (11%) patients were positive for T (6 patients not surgically treated; 4 patients with local recurrence after surgery) and N (lymph-nodal disease); 5/94 (5%) patients were positive for T and M (metastatic bone disease), 14/94 (15%) patients for N and M, 16/94 (17%) patients were positive only for T, 15/94 (16%) patients only for N, and 27/94 (29%) patients only for M. After a median FU of 26 months (range 13– 52), 52 (55%) patients had PD, and 42 (45%) showed SD.

The 134 most [^{18}F]Cho-avid lesions in all 94 patients were selected (T = 38; N = 44; M = 52) for texture analysis and ML feature classification. After the statistical reduction and selection process, we identified the following features able to discriminate the occurrence of disease progression at follow-up:

For the whole group (N = 94), 2 features (HISTO_Entropy_log10; HISTO_Energy_Uniformity) with sensitivity 47.1%, specificity 76.6%, and accuracy 67.7% (**figure 9**).

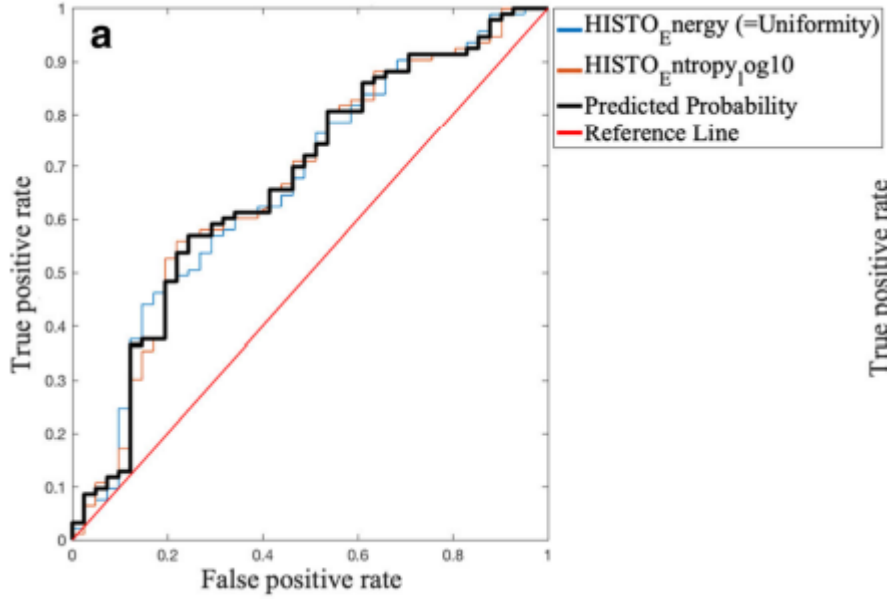


Figure 9. ROC curve analysis for significant features in the outcome prediction in BCR PCa (from [13]).

We also obtained better results considering the T-only (accuracy 87%), N-only (accuracy 82.5%) and M-only (accuracy 72.5%). However, such results may be misleading due to the samples' reduction.

Discussion

The first aim of this study was to confirm [12] the potential application of texture analysis on [^{18}F]Cho-PET/CT images in BCR PCa. We tried to obtain a more rigorous radiomics study through the following steps: (1) acquisition of image data, (2) segmentation of target regions, (3) feature extraction, (4) feature reduction, and (5) identification of the prediction model. Consequently, many challenges must be addressed. First, the quality of radiomics studies depends on the imaging characteristics and, for this reason, the degree of image standardization must be as high as possible. To solve this challenge, our study is based on a real-life scenario with a standardized mono-centric dataset of 94 patients undergoing [^{18}F]Cho-PET/CT imaging scans performed using the same scanner and the same standard whole-body oncological protocol. Second, an operator-independent segmentation method must be used to extract target regions. Although manual delineation seems like the most intuitive and easily

implemented way of obtaining target volume, it is operator-dependent thus producing less precise and, mainly, irreproducible results. Consequently, we used an innovative user-independent segmentation algorithm based on active contours, as described in [40], where the segmentation is applied on separate 2D PET slices to obtain the whole 3D volume: this is a very convenient and efficient oversimplification. Nevertheless, a more powerful and coherent procedure could be performed on 3D slices simultaneously by evolving a single surface within the corresponding 3D space. Also, further improvements consist of combining a ML approach with the active contour to consider the tissue classification [41]. Then, we used an IBSI-compliant software for feature extraction (Lifex [30]), and then we used the DA as solid statistical classifier to create the predictive model. Indeed, the DA seems to provide better results in the PET tissue classification with respect to other classifiers as already described [41]. Third, an ad hoc high-throughput analysis tool must be used to automatically extract features.

So far and in a new scenario, only another study in the literature assessed the role of ML radiomics Cho-PET in the prediction of PCa patients' outcome. The study was also from our group and included a smaller cohort of PCa patients ($n = 38$), reaching, however, similar accuracy confirming the suboptimal results of the presented study (66% vs 67.7%) but considering 13 features [12]. This experience contains some limitations (retrospective study, heterogeneous treatment, missing external validation). Nonetheless, we hope that our preliminary and suboptimal results will provide the basis for future prospective studies to provide new and crucial information on risk stratification of PCa patients independently to classic staging systems and/or clinical, radiological findings.

3. Deep learning experiences

3.1 Brain - Unsupervised Brain Segmentation System Using K-Means and CNN [15]

Background

Voxel-Based Morphometry (VBM) is a technique able to further characterize the anatomy also of the brain [42]. Indeed, after the segmentation and differentiation of constituent parts, VBM aims to determine if a specific voxel has a different intensity more similar to one group instead of another, correlating morpho-volumetric variations and allowing to compare results between pathological subjects and healthy controls or longitudinal comparisons. VBM brain's analysis is mainly based on MRI signal intensity (gold standard for dementia), usually weighted in T1 or T2 sequences that can be affected by several issues, i.e. noise, the intensity of non-uniform tissue, and partial volume effect [43]. For this reason, a robust method of brain voxel classification is mandatory. Also, the radiomics feature extraction process from biomedical images depends on a reliable volume segmentation [13] which is, therefore, a prerequisite for obtaining accurate and reproducible parameters associated with the target tissue. Most of the used computer-aided design (CAD) tools for brain analysis are performed using the Functional brain MRI (FMRIB) Software Library (FSL) and SPM [44]. Such tools provide a satisfactory VBM analysis but are both related to the setup of a high number of parameters that can lead to different and/or inaccurate segmentation results. The search for the most accurate parameters able to obtain quantitative results more similar to the gold standard can be made through several manual attempts, representing a time-loss methodology with intra- and inter-operator result variability.

Therefore, the aim of this study was to present a novel VBM analysis system able to segment MRI 3D brain volume without user intervention and parameters setting, thus overcoming such limitations.

Methods

Briefly, a CNN has been trained using the voxels classified by an unsupervised k-means algorithm using the different intensity distribution of tissue signals. brain Then, the trained CNN is employed for segmentation purposes to discriminate among white matter (WM), grey matter (GM) and CSF. The obtained segmentations are finally compared with FSL and SPM results. The proposed method aimed to segment a whole-brain T1 MRI study automatically, classifying each voxel in CSF, GM and WM as resumed in **figure 10**.

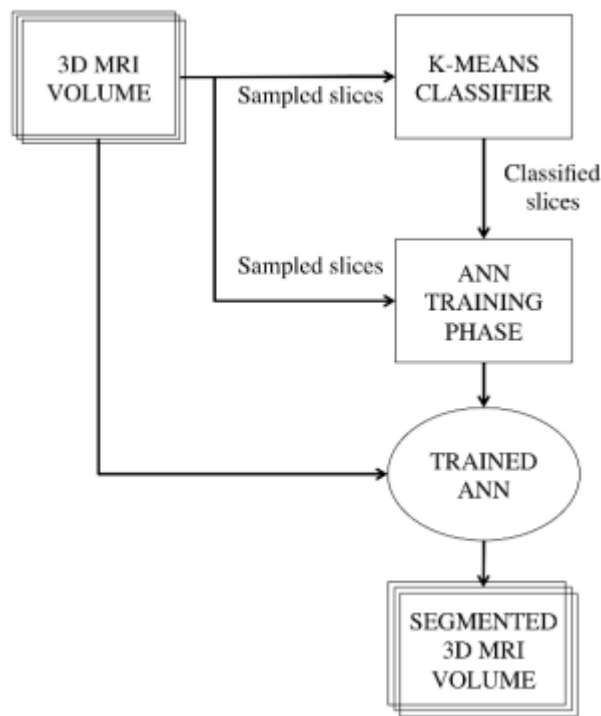


Figure 10. The workflow of the proposed method (from [15]).

The system considered as input an MRI dataset (hundreds of slices, generally 50~300, in DICOM format of 256 x 256 voxels). The dataset was then sampled considering a group of only 3 slices as training set: one slice was selected near the neck zone, where the brain starts and the presence of the CSF matter is predominant with respect to GM and WM; one slice in the middle of the sequence, where WM and GM are little predominant with respect to CSF; the last slice was chosen in the upper section of the brain, where the WM is more prominent than the other two. These slices are the input of the k-means clustering algorithm: with $k = 3$

clusters, the k-means assigns each voxel to a cluster, labelling it with the cluster number (1 = CSF, 2 = GM, 3 = WM). Because of the nature of the k-means, labels are randomly assigned to the clusters: each group is then re-labelled according to the centroid value of each cluster. As a matter of fact, in the T1 sequence, the CSF has small intensity values, the WM has the highest intensity values, and the GM has a mean intensity (between the CSF and WM). The CNN training set is the combination of the input set (voxel intensity values) and the target set (voxel labels). When the training phase is completed, the trained CNN can segment and classify each voxel of the whole brain volume. Each segmented voxel can be a:

- TP: a voxel considered the same tissue (CSF or GM or WM) both in reference and in calculated segmentation;
- FP: a voxel considered belonging to a tissue (CSF or GM or WM) but not considered as such in the reference segmentation;
- FN: a voxel that is excluded from a tissue (CSF or GM or WM) but considered to belong to that tissue in the reference segmentation;
- TN: a voxel excluded both from the reference and calculated segmentation.

The performance was evaluated using the dice similarity coefficient (DSC) as follows:

$$DSC = (2*TP)/(2*TP+FN+FP)$$

The dataset has been segmented using the proposed methodology and the results have been compared with FSL and SPM results.

Results

In this experience we assessed a public MRI brain cohort from the Internet Brain Segmentation Repository (IBSR) dataset (v2.0) [45] composed of 18 brain T1-weighted acquisitions; volumes were already skull stripped, and the dataset is provided with a reference segmentation

made by expert radiologists, used to evaluate the precision of the segmentation methodologies. For each patient, a series of three slices have been sampled with the k-means algorithm and used as the training set for the CNN. The hidden layer of the proposed CNN was composed of 30 neurons; the output layer was composed of 3 neurons, one for each output tissue. The training of the CNN needed less than a minute, while the segmentation of the whole volume needed just a couple of seconds. Then, the segmentations have been compared with the reference segmentations, also in terms of DSC. The segmentation has been carried out also using FSL and SPM with default parameters. The obtained DSC results for all segmentation methodologies are shown in **table 2**.

	CSF	GM	WM
FSL	53,3±5,5	78,1±2,5	87,1±3,0
SPM	40,8±4,3	79,8±5,3	85,8±2,3
Our system	65,4±7,6	83,7±4,1	86,2±2,2

Table 2. DSC for segmentations obtained using FSL, SPM, and the proposed system (from [15]).

The DSC considered both corrected and uncorrected labelled voxels, showing a general improvement of the proposed system if compared to FSL and SPM, despite WM for FSL. Also, the proposed unsupervised system resulted faster and without the need to set any parameter: the segmentation of the whole dataset, composed of 18 x (256*256*128) voxels, needed 504 seconds for FSL, 652 seconds for SPM, and 162 seconds for the proposed method.

Discussion

The ability to segment brain tissues accurately from MRI can magnify the utility of this fundamental neuroimaging technique. Manual contouring is still a common choice in clinical practice despite limitations, and for this reason, several computer-aided segmentation systems supporting automatic or semi-automatic algorithms have been proposed [46]. In this study, a novel unsupervised system that uses a k-means classifier and a CNN has been proposed, resulting fast and reliable, also in comparison with other state-of-the-art segmentation systems

[44, 47]. Our system sampled a small amount of data from the whole volume that was classified using the k-means algorithm. Classified voxels were then used as the training set for the feed-forward CNN, which learned the segmentation phase. Each voxel of the whole volume was then segmented using the trained CNN, obtaining superior results if compared to FSL and SPM, as shown in **table 2**. Therefore, the proposed system could be used as a CDSS to help clinicians in treatment response evaluation of neurological diseases in terms of brain's components volumes variations [48]. Indeed, despite limitations, our system reached reasonable segmentations of WM, GM and CSF based on standard MRI potentially representing a base for additional, more complex, and complete segmentation procedures for tasks such as the automated labelling of brain areas.

3.2 Prostate – Deep learning prediction of PSMA PET prostatic volume based on T2 MRI

Background

ML approaches in PCa have shown promising results with different tracers in molecular profiling [49], lesion characterization with disease outcome prediction [13, 50], and survival assessment [12]. Furthermore, AI has been used in several steps from technical, such as automatic segmentation [51], dose and scanning time reduction [52], to clinical applications for lesion detection [53]. Prostate-specific membrane antigen (PSMA) PET is a relatively new and game-changing modality able to improve PCa assessment, from diagnosis to restaging [54, 55]. Simultaneous PSMA PET/MRI enables the unique opportunity to assess the added value of multiparametric (mp) MRI (mpMRI) with this novel PET tracer for the detection of PCa. Indeed, several studies suggested an increase in accuracy detection for significant PCa (sig PCa) if PSMA PET data are combined with the morphological information from T2 sequences compared to mpMRI alone [56]. This technology however is not widely available and is still limited to a few centers mainly due to high costs. The applications of ML and AI on simultaneous PSMA PET/MRI may further improve the use and the evidence of such a unique state-of-the-art technique in several aspects of PCa: from segmentation to accurate analysis and correlation through unconventional parameters. But how far can we go with AI? We asked ourselves if it is possible to further enhance AI applications in PCa molecular imaging improving the diagnostic confidence in mpMRI. Therefore, we preliminarily assessed the feasibility of CNN prediction of PSMA prostatic distribution based on T2-MRI images acquired from simultaneous PSMA PET/MRI.

Methods

In this retrospective study, we screened all PCa patients who, between 01.04.2016 and 01.12.2020, consecutively underwent a staging (n = 177) or prospectively biopsy-guidance for PCa (n = 45) PSMA PET/MRI at the nuclear medicine department of the Universitatsspital Zurich (USZ, Switzerland). Then, we excluded patients who previously underwent

locoregional therapies (n = 34) or without any PSMA prostatic uptake (n = 11). The study was approved by the institutional review board (2020-02861); all staging patients signed a general informed consent for retrospective studies, while biopsy guidance patients signed the specific written informed consent of the prospective study.

All patients underwent [^{68}Ga]Ga-PSMA-11 or [^{18}F]PSMA-1007 PET/MRI scans (SIGNA PET/3T MRI, GE Healthcare, Waukesha, WI, USA). Images were acquired starting with a whole-body MRI localizer scan. Subsequently, a 3D dual-echo, spoiled gradient recalled echo sequence (LAVA-FLEX) for attenuation correction, and a PET emission scan were acquired (60 and 90 min after the injection of [^{68}Ga]Ga-PSMA-11 or [^{18}F]PSMA-1007, respectively) as extensively described in [57].

For each patient, using 3D Slicer [58] I manually segmented the T2 MRI images of the prostatic gland including seminal vesicles. These volumes were then confirmed by a double board-certified radiologist and nuclear medicine physician with 12 years of experience. Then, the prostatic beds on PSMA PET scans were segmented through Lifex [30] and considered as the standard of reference: to increase the specificity of our predictive model, we considered an SUV threshold greater than 5 to generate positive and negative voxels. An SUV cut-off of 4 was used in patients without PSMA prostatic uptake greater than 5 and considered as validation. Then, T2 weighted axial sequences were semiautomatically segmented to select the prostate volume. Finally, a CNN was trained on the T2 images to generate a predictive prostatic PSMA PET map.

Results

One hundred seventy-seven (177) patients (mean age 65.9 ± 7.9 years) with a median PSA of 10.1 ng/ml (1.28 – 480) underwent [^{68}Ga]Ga-PSMA-11 (154/177) or [^{18}F]PSMA-1007 (23/177) PET/MRI with an administered median dose of 124 MBq [76 – 198] or 239 MBq [135 – 303], respectively. Clinically sig PCa at biopsy was present in 145/177 of them (81.9%). 34 patients had no PSMA uptake > 5 ; therefore, they were re-segmented with an SUV > 4 and

used as validation. In this way, the reached DSC by our model was $69.47 \pm 15.62\%$ as represented in **figure 11**.

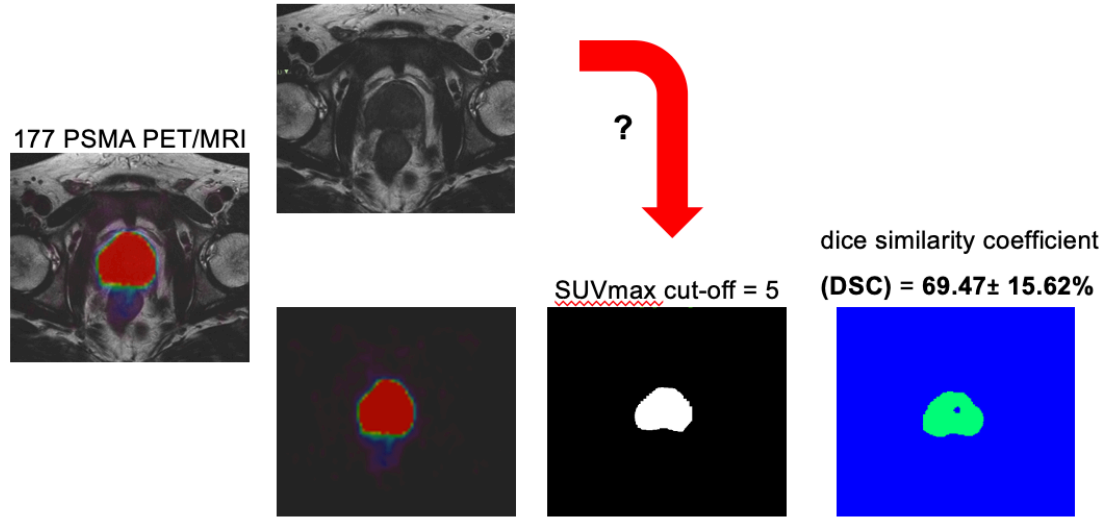


Figure 11. An illustrative representation of the proposed method.

Discussion

Despite several applications of AI in medical imaging, there is no data in the literature comparable to the presented preliminary DL experience. In my eyes, AI can also offer opportunities to reduce potential gaps between hospitals with and without high-level facilities, and among nations with different rules. Indeed, patients worldwide with suspicious PCa have easily access to pelvic MRI; however, we cannot affirm the same for PSMA PET which is a relatively new and game-changing modality able to improve PCa assessment, from diagnosis to restaging. The opportunity to consider also the PSMA prostatic distribution for each patient undergoing a prostate MRI could improve, in a futuristic vision, the physicians' confidence potentially confirming/invalidating any unclear/doubtful MRI findings. Accordingly, we have shown that based only on the T2 MRI, increased prostatic PSMA uptake can be estimated in staging PCa reaching a DSC of $69.47 \pm 15.62\%$. Further investigation with larger cohorts and

external validation are warranted to assess whether PSMA uptake can be predicted accurately enough to help in the interpretation of mpMRI.

4. Conclusion

In my eyes, it is time to produce and deliver more robust evidence accelerating the use of the various facets of AI applications in clinical practice. Indeed, ML and DL can perform tasks that are normal characteristics of human intelligence, making autonomous decisions based on the collection of data and reducing the daily workflow timing. ML and DL can also help to reduce the fundamental but vast amount of radiomics data that may magnify the whole imaging assessment considering every single pixel/voxel features that are not assessable by the human eye. All these techniques are receiving growing attention from the scientific community worldwide in different pathologies. As we confirmed also in this thesis, there are several potential applications in the clinical scenario from image interpretation to outcome and response to therapy prediction. As demonstrated, AI also has the potential to optimize timing, potentially reducing costs, and interobserver variations. Furthermore, I preliminary showed that AI (DL) may also predict the results of a costly examination resulting useful in less-advanced countries worldwide and potentially enhancing physicians' confidence and patients' quality of life (also reducing the radiation burden). However, data availability, privacy concerns, and lack of transparent, standardized, and universal procedural agreements are limiting the development of AI approaches. But there are preliminary attempts to override these limitations, and fully automated processing and high-level computer interpretation of imaging are nowadays becoming a reality.

What should we expect then?

Molecular imaging and AI are both growing faster. Building big databases containing clinical and image data is the next but essential step in creating and training automated diagnostic/prognostic models able to help clinicians to make unbiased and faster decisions for precision healthcare. Deep and multicentric collaborations are, therefore, warranted: it is fundamental to deliver (and confirm) more evidence in the literature to further accelerate the

use of artificial intelligence applications as well as the diffusion of new diagnostic and therapeutic approaches. AI applications will be essential to handle and integrate the vast amounts of quantitative data generated for each exam with clinical data to facilitate a shift towards more personalized medicine. At the end of the path, medical doctors will probably play a role as supervisors of automatically generated data, given their capability to integrate data based on their clinical experience. Therefore, physicians will remain ultimately responsible for patient care and will need to acquire new skills to do their best for patients in the new AI ecosystem.

5. Abbreviations' list

AD Alzheimer's disease

AI artificial intelligence

AUC ROC area under the receiver operating characteristics curve

BCR biochemical recurrence

CAD computer-aided design

CDSS clinical decision support system

ceCT contrast enhancement computer tomography

CgA chromogranin A

CI confidence interval

CNN convolutional neural network

CR complete response

CRC colorectal cancer

CSF cerebrospinal fluid

CT computed tomography

DA discriminant analysis

DICOM digital imaging and communications in medicine

DL deep learning

DSC dice similarity coefficient

EOAD early-onset Alzheimer's disease

FBB florbetaben

FDG fluorodeoxyglucose

FN false-negative

FP false-positive

FSL Functional brain MRI (FMRIB) Software Library

FU follow-up

GEP gastroenteropancreatic

GM grey matter

IBSI image biomarker standardisation initiative

MCI mild cognitive impairment

MDT multidisciplinary team

ML machine learning

MMSE mini-mental state examination

mpMRI multiparametric MRI

MRI magnetic resonance imaging

NETs neuroendocrine tumors

PBC point biserial correlation

PCa prostate cancer

PD progressive disease

PET positron emission tomography

PR partial response

PSA prostate-specific antigen

PSMA prostate-specific membrane antigen

RLT radioligand therapy

ROI regions of interest

RPE radical prostatectomy

RT radiotherapy

SD stable disease

sig PCa clinically significant PCa

SPM Statistical Parametric Mapping

SSTR somatostatin receptor

SUV_{max} maximum standardized uptake value

SVM support vector machine

TP true-positive

TV true-negative

VBM voxel-based morphometry

VOI volume of interest

WM white matter

6. References

1. Laudicella R, Comelli A, Stefano A, Szostek M, Crocè L, Vento A, Spataro A, Comis AD, La Torre F, Gaeta M, Baldari S, Alongi P. Artificial Neural Networks in Cardiovascular Diseases and its Potential for Clinical Application in Molecular Imaging. *Curr Radiopharm.* 2021;14(3):209-219
2. Laudicella R, Iagaru A, Comelli A, Baldari S, Burger IA. Artificial Intelligence Clinical Application in Prostate Cancer Molecular Imaging. *healthbook TIMES Oncology Hematology.* 2021;7(1):28-35
3. Popescu C, Laudicella R, Baldari S, Alongi P, Burger I, Comelli A, Caobelli F. PET-based artificial intelligence applications in cardiac nuclear medicine. *Swiss Med Wkly.* 2022 Jan 27;152:w30123
4. Liberini V, Laudicella R, Balma M, Nicolotti DG, Buschiazio A, Grimaldi S, Lorenzon L, Bianchi A, Peano S, Bartolotta TV, Farsad M, Baldari S, Burger IA, Huellner MW, Papaleo A, Deandrei D. Radiomics and artificial intelligence in prostate cancer: new tools for molecular hybrid imaging and theragnostics. *Eur Radiol Exp.* 2022 Jun 15;6(1):27
5. Zukotynski K, Gaudet V, Uribe CF, Mathotaarachchi S, Smith KC, Rosa-Neto P, Bénard F, Black SE. Machine Learning in Nuclear Medicine: Part 2-Neural Networks and Clinical Aspects. *J Nucl Med.* 2021 Jan;62(1):22-29
6. Jha AK, Bradshaw TJ, Buvat I, Hatt M, Kc P, Liu C, Obuchowski NF, Saboury B, Slomka PJ, Sunderland JJ, Wahl RL, Yu Z, Zuehlsdorff S, Rahmim A, Boellaard R. Nuclear Medicine and Artificial Intelligence: Best Practices for Evaluation (the RELAINCE guidelines). *J Nucl Med.* 2022 May 26;jnumed.121.263239
7. Slart RHJA, Williams MC, Juarez-Orozco LE, Rischpler C, Dweck MR, Glaudemans AWJM, Gimelli A, Georgoulas P, Gheysens O, Gaemperli O, Habib G, Hustinx R, Cosyns B, Verberne HJ, Hyafil F, Erba PA, Lubberink M, Slomka P, Išgum I, Visvikis D, Kolossváry M, Saraste A. Position paper of the EACVI and EANM on artificial intelligence applications in multimodality cardiovascular imaging using SPECT/CT, PET/CT, and cardiac CT. *Eur J Nucl Med Mol Imaging.* 2021 May;48(5):1399-1413
8. Laudicella R, Bauckneht M, Cuppari L, Donegani MI, Arnone A, Baldari S, Burger IA, Quartuccio N. Emerging applications of imaging in glioma: focus on PET/MRI and radiomics. *Clin Transl Imaging* 2021 9, 609–623

9. Quartuccio N, Marrale M, Laudicella R, Alongi P, Siracusa M, Sturiale L, Arnone A, Cutaia G, Salvaggio G, Midiri M, Baldari S, Arnone G. The role of PET radiomic features in prostate cancer: a systematic review. *Clin Transl Imaging* 2021 9, 579–588
10. Alongi P, Laudicella R, Panasiti F, Stefano A, Comelli A, Giaccone P, Arnone A, Minutoli F, Quartuccio N, Cupidi C, Arnone G, Piccoli T, Grimaldi LME, Baldari S, Russo G. Radiomics Analysis of Brain [18F]FDG PET/CT to Predict Alzheimer's Disease in Patients with Amyloid PET Positivity: A Preliminary Report on the Application of SPM Cortical Segmentation, Pyradiomics and Machine-Learning Analysis. *Diagnostics (Basel)*. 2022 Apr 8;12(4):933
11. Alongi P, Stefano A, Comelli A, Spataro A, Formica G, Laudicella R, Lanzafame H, Panasiti F, Longo C, Midiri F, Benfante V, La Grutta L, Burger IA, Bartolotta TV, Baldari S, Lagalla R, Midiri M, Russo G. Artificial Intelligence Applications on Restaging [18F]FDG PET/CT in Metastatic Colorectal Cancer: A Preliminary Report of Morpho-Functional Radiomics Classification for Prediction of Disease Outcome. *Applied Sciences*. 2022; 12(6):2941
12. Alongi P, Laudicella R, Stefano A, Caobelli F, Comelli A, Vento A, Sardina D, Ganduscio G, Toia P, Ceci F, Mapelli P, Picchio M, Midiri M, Baldari S, Lagalla R, Russo G. Choline PET/CT features to predict survival outcome in high risk prostate cancer restaging: a preliminary machine-learning radiomics study. *Q J Nucl Med Mol Imaging*. 2020 Jun 15
13. Alongi P, Stefano A, Comelli A, Laudicella R, Scalisi S, Arnone G, Barone S, Spada M, Purpura P, Bartolotta TV, Midiri M, Lagalla R, Russo G. Radiomics analysis of 18F-Choline PET/CT in the prediction of disease outcome in high-risk prostate cancer: an explorative study on machine learning feature classification in 94 patients. *Eur Radiol*. 2021 Jul;31(7):4595-4605
14. Laudicella R, Comelli A, Liberini V, Vento A, Stefano A, Spataro A, Crocè L, Baldari S, Bambaci M, Deandrei D, Arico' D, Ippolito M, Gaeta M, Alongi P, Minutoli F, Burger IA, Baldari S. [68Ga]DOTATOC PET/CT Radiomics to Predict the Response in GEP-NETs Undergoing [177Lu]DOTATOC PRRT: The "Theragnostics" Concept. *Cancers (Basel)*. 2022 Feb 16;14(4):984
15. Laudicella, R., Agnello, L., Comelli, A. (2022). Unsupervised Brain Segmentation System Using K-Means and Neural Network. In: Mazzeo, P.L., Frontoni, E., Sclaroff, S.,

Distante, C. (eds) Image Analysis and Processing. ICIAP 2022 Workshops. ICIAP 2022. Lecture Notes in Computer Science, vol 13373. Springer

16. Castellani RJ, Rolston RK, Smith MA. Alzheimer disease. *Dis Mon.* 2010 Sep;56(9):484-546

17. Jack CR Jr, Bennett DA, Blennow K, Carrillo MC, Dunn B, Haeberlein SB, Holtzman DM, Jagust W, Jessen F, Karlawish J, Liu E, Molinuevo JL, Montine T, Phelps C, Rankin KP, Rowe CC, Scheltens P, Siemers E, Snyder HM, Sperling R; Contributors. NIA-AA Research Framework: Toward a biological definition of Alzheimer's disease. *Alzheimers Dement.* 2018 Apr;14(4):535-562

18. Sorbi S, Hort J, Erkinjuntti T, Fladby T, Gainotti G, Gurvit H, Nacmias B, Pasquier F, Popescu BO, Rektorova I, Religa D, Rusina R, Rossor M, Schmidt R, Stefanova E, Warren JD, Scheltens P; EFNS Scientist Panel on Dementia and Cognitive Neurology. EFNS-ENS Guidelines on the diagnosis and management of disorders associated with dementia. *Eur J Neurol.* 2012 Sep;19(9):1159-79

19. Ashburner J, Friston KJ. Unified segmentation. *Neuroimage.* 2005 Jul 1;26(3):839-51

20. Fornacon-Wood I, Mistry H, Ackermann CJ, Blackhall F, McPartlin A, Faivre-Finn C, Price GJ, O'Connor JPB. Reliability and prognostic value of radiomic features are highly dependent on choice of feature extraction platform. *Eur Radiol.* 2020 Nov;30(11):6241-6250

21. Fornacon-Wood I, Mistry H, Ackermann CJ, Blackhall F, McPartlin A, Faivre-Finn C, Price GJ, O'Connor JPB. Reliability and prognostic value of radiomic features are highly dependent on choice of feature extraction platform. *Eur Radiol.* 2020 Nov;30(11):6241-6250

22. Barone S, Cannella R, Comelli A, Pellegrino A, Salvaggio G, Stefano A, Vernuccio F. Hybrid descriptive-inferential method for key feature selection in prostate cancer radiomics. *Appl. Stoch. Model. Bus. Ind.* 2021;37:961–972

23. Comelli A, Stefano A, Bignardi S, Russo G, Sabini MG, Ippolito M, Barone S, Yezzi A. Active contour algorithm with discriminant analysis for delineating tumors in positron emission tomography. *Artif. Intell. Med.* 2019;94:67–78

24. Zhou H, Jiang J, Lu J, Wang M, Zhang H, Zuo C; Alzheimer's Disease Neuroimaging Initiative. Dual-Model Radiomic Biomarkers Predict Development of Mild Cognitive Impairment Progression to Alzheimer's Disease. *Front Neurosci.* 2019 Jan 11;12:1045

25. Li Y, Jiang J, Lu J, Jiang J, Zhang H, Zuo C. Radiomics: A novel feature extraction method for brain neuron degeneration disease using 18F-FDG PET imaging and its implementation for Alzheimer's disease and mild cognitive impairment. *Ther. Adv. Neurol. Disord.* 2019;12:1756286419838682
26. Jiang J, Wang M, Alberts I, Sun X, Li T, Rominger A, Zuo C, Han Y, Shi K, Initiative F.T.A.D.N. Using radiomics-based modelling to predict individual progression from mild cognitive impairment to Alzheimer's disease. *Eur. J. Pediatr.* 2022:1–11
27. Zhou P, Zeng R, Yu L, Feng Y, Chen C, Li F, Liu Y, Huang Y, Huang Z, Initiative T.A.D.N. Deep-Learning Radiomics for Discrimination Conversion of Alzheimer's Disease in Patients with Mild Cognitive Impairment: A Study Based on 18F-FDG PET Imaging. *Front. Aging Neurosci.* 2021;13:764872
28. Sung H, Ferlay J, Siegel RL, Laversanne M, Soerjomataram I, Jemal A, Bray F. Global Cancer Statistics 2020: GLOBOCAN Estimates of Incidence and Mortality Worldwide for 36 Cancers in 185 Countries. *CA Cancer J. Clin.* 2021, 71, 209–249
29. Chen SW, Shen WC, Chen WT, Hsieh TC, Yen KY, Chang JG, Kao CH. Metabolic Imaging Phenotype Using Radiomics of [¹⁸F]FDG PET/CT Associated with Genetic Alterations of Colorectal Cancer. *Mol Imaging Biol.* 2019 Feb;21(1):183-190
30. Nioche C, Orlhac F, Boughdad S, Reuzé S, Goya-Outi J, Robert C, Pellot-Barakat C, Soussan M, Frouin F, Buvat I. LIFEx: A Freeware for Radiomic Feature Calculation in Multimodality Imaging to Accelerate Advances in the Characterization of Tumor Heterogeneity. *Cancer Res.* 2018 Aug 15;78(16):4786-4789
31. Van Helden EJ, Vacher YJL, van Wieringen WN, van Velden FHP, Verheul HMW, Hoekstra OS, Boellaard R, Menke-van der Houven van Oordt CW. Radiomics analysis of pre-treatment [¹⁸F]FDG PET/CT for patients with metastatic colorectal cancer undergoing palliative systemic treatment. *Eur. J. Nucl. Med. Mol. Imaging.* 2018, 45, 2307–2317
32. Bundschuh RA, Dinges J, Neumann L, Seyfried M, Zsótér N, Papp L, Rosenberg R, Becker K, Astner ST, Henninger M, Herrmann K, Ziegler SI, Schwaiger M, Essler M. Textural Parameters of Tumor Heterogeneity in ¹⁸F-FDG PET/CT for Therapy Response Assessment and Prognosis in Patients with Locally Advanced Rectal Cancer. *J Nucl Med.* 2014 Jun;55(6):891-7

33. Hennrich U, Kopka K. Lutathera[®]: The First FDA- and EMA-Approved Radiopharmaceutical for Peptide Receptor Radionuclide Therapy. *Pharmaceuticals (Basel)*. 2019 Jul 29;12(3):114
34. Oberg K, Krenning E, Sundin A, Bodei L, Kidd M, Tesselaar M, Ambrosini V, Baum RP, Kulke M, Pavel M, Cwikla J, Drozdov I, Falconi M, Fazio N, Frilling A, Jensen R, Koopmans K, Korse T, Kwekkeboom D, Maecke H, Paganelli G, Salazar R, Severi S, Strosberg J, Prasad V, Scarpa A, Grossman A, Walenkamp A, Cives M, Virgolini I, Kjaer A, Modlin IM. A Delphic consensus assessment: imaging and biomarkers in gastroenteropancreatic neuroendocrine tumor disease management. *Endocr Connect*. 2016 Sep;5(5):174-87
35. Spada F, Campana D, Lamberti G, Laudicella R, Dellamano R, Dellamano L, Leeuwenkamp O, Baldari S. [¹⁷⁷Lu]Lu-DOTA-TATE versus standard of care in adult patients with gastro-enteropancreatic neuroendocrine tumours (GEP-NETs): a cost-consequence analysis from an Italian hospital perspective. *Eur J Nucl Med Mol Imaging*. 2022 May;49(6):2037-2048
36. Weber M, Kessler L, Schaarschmidt B, Fendler WP, Lahner H, Antoch G, Umutlu L, Herrmann K, Rischpler C. Treatment-related changes in neuroendocrine tumors as assessed by textural features derived from ⁶⁸Ga-DOTATOC PET/MRI with simultaneous acquisition of apparent diffusion coefficient. *BMC Cancer*. 2020 Apr 16;20(1):326.
37. Önnér H, Abdülrezzak Ü, Tutuş A. Could the skewness and kurtosis texture parameters of lesions obtained from pretreatment Ga-68 DOTA-TATE PET/CT images predict receptor radionuclide therapy response in patients with gastroenteropancreatic neuroendocrine tumors? *Nucl Med Commun*. 2020 Oct;41(10):1034-1039
38. Siegel RL, Miller KD, Fuchs HE, Jemal A. Cancer Statistics, 2021. *CA Cancer J Clin*. 2021;71(1):7-33
39. Kumar V, Gu Y, Basu S, Berglund A, Eschrich SA, Schabath MB, Forster K, Aerts HJ, Dekker A, Fenstermacher D, Goldgof DB, Hall LO, Lambin P, Balagurunathan Y, Gatenby RA, Gillies RJ. Radiomics: the process and the challenges. *Magn Reson Imaging*. 2012 Nov;30(9):1234-48
40. Comelli A, Stefano A, Russo G, Sabini MG, Ippolito M, Bignardi S, Petrucci G, Yezzi A. A smart and operator independent system to delineate tumours in Positron Emission Tomography scans. *Comput Biol Med*. 2018 Nov 1;102:1-15

41. Comelli A, Bignardi S, Stefano A, Russo G, Sabini MG, Ippolito M, Yezzi A. Development of a new fully three-dimensional methodology for tumours delineation in functional images. *Comput Biol Med.* 2020 May;120:103701
42. Kennedy DN, Filipek PA, Caviness VR. Anatomic segmentation and volumetric calculations in nuclear magnetic resonance imaging. *IEEE Trans Med Imaging.* 1989;8(1):1-7
43. Stefano A, Gallivanone F, Messa C, Gilardi MC, Gastiglioni I. Metabolic impact of partial volume correction of [18F]FDG PET-CT oncological studies on the assessment of tumor response to treatment. *Q J Nucl Med Mol Imaging.* 2014 Dec;58(4):413-23
44. Woolrich MW, Jbabdi S, Patenaude B, Chappell M, Makni S, Behrens T, Beckmann C, Jenkinson M, Smith SM. Bayesian analysis of neuroimaging data in FSL. *Neuroimage.* 2009 Mar;45(1 Suppl):S173-86
45. Rohlfing T. Image similarity and tissue overlaps as surrogates for image registration accuracy: widely used but unreliable. *IEEE Trans Med Imaging.* 2012 Feb;31(2):153-63
46. Russo G, Stefano A, Alongi P, Comelli A, Catalfamo B, Mantarro C, Longo C, Altieri R, Certo F, Cosentino S, Sabini MG, Richiusa S, Barbagallo GMV, Ippolito M. Feasibility on the Use of Radiomics Features of 11[C]-MET PET/CT in Central Nervous System Tumours: Preliminary Results on Potential Grading Discrimination Using a Machine Learning Model. *Curr Oncol.* 2021 Dec 12;28(6):5318-5331
47. Dora L, Agrawal S, Panda R, Abraham A. State-of-the-Art Methods for Brain Tissue Segmentation: A Review. *IEEE Rev Biomed Eng.* 2017;10:235-249
48. Alongi P, Sardina DS, Coppola R, Scalisi S, Puglisi V, Arnone A, Raimondo GD, Munerati E, Alaimo V, Midiri F, Russo G, Stefano A, Giugno R, Piccoli T, Midiri M, Grimaldi LME. 18F-Florbetaben PET/CT to Assess Alzheimer's Disease: A new Analysis Method for Regional Amyloid Quantification. *J Neuroimaging.* 2019 May;29(3):383-393
49. Papp L, Spielvogel CP, Grubmüller B, Grahovac M, Krajnc D, Ecsedi B, Sareshgi RAM, Mohamad D, Hamboeck M, Rausch I, Mitterhauser M, Wadsak W, Haug AR, Kenner L, Mazal P, Susani M, Hartenbach S, Baltzer P, Helbich TH, Kramer G, Shariat SF, Beyer T, Hartenbach M, Hacker M. Supervised machine learning enables non-invasive lesion characterization in primary prostate cancer with [68Ga]Ga-PSMA-11 PET/MRI. *Eur J Nucl Med Mol Imaging.* 2021 Jun;48(6):1795-1805

50. Moazemi S, Erle A, Khurshid Z, Lütje S, Muders M, Essler M, Schultz T, Bundschuh RA. Decision-support for treatment with ¹⁷⁷Lu-PSMA: machine learning predicts response with high accuracy based on PSMA-PET/CT and clinical parameters. *Ann Transl Med*. 2021 May;9(9):818
51. Johnsson K, Brynolfsson J, Sahlstedt H, Nickols NG, Rettig M, Probst S, Morris MJ, Bjartell A, Eiber M, Anand A. Analytical performance of aPROMISE: automated anatomic contextualization, detection, and quantification of [¹⁸F]DCFPyL (PSMA) imaging for standardized reporting. *Eur J Nucl Med Mol Imaging*. 2022 Feb;49(3):1041-1051
52. Wang YJ, Baratto L, Hawk KE, Theruvath AJ, Pribnow A, Thakor AS, Gatidis S, Lu R, Gummidipundi SE, Garcia-Diaz J, Rubin D, Daldrup-Link HE. Artificial intelligence enables whole-body positron emission tomography scans with minimal radiation exposure. *Eur J Nucl Med Mol Imaging*. 2021 Aug;48(9):2771-2781
53. Zhao Y, Gafita A, Vollnberg B, Tetteh G, Haupt F, Afshar-Oromieh A, Menze B, Eiber M, Rominger A, Shi K. Deep neural network for automatic characterization of lesions on ⁶⁸Ga-PSMA-11 PET/CT. *Eur J Nucl Med Mol Imaging*. 2020 Mar;47(3):603-613
54. Rüschoff JH, Ferraro DA, Muehlematter UJ, Laudicella R, Hermanns T, Rodewald AK, Moch H, Eberli D, Burger IA, Rupp NJ. What's behind ⁶⁸Ga-PSMA-11 uptake in primary prostate cancer PET? Investigation of histopathological parameters and immunohistochemical PSMA expression patterns. *Eur J Nucl Med Mol Imaging*. 2021 Nov;48(12):4042-4053
55. Ferraro DA, Laudicella R, Zeimpekis K, Mebert I, Müller J, Maurer A, Grünig H, Donati O, Sapienza MT, Rueschoff JH, Rupp N, Eberli D, Burger IA. Hot needles can confirm accurate lesion sampling intraoperatively using [¹⁸F]PSMA-1007 PET/CT-guided biopsy in patients with suspected prostate cancer. *Eur J Nucl Med Mol Imaging*. 2022 Apr;49(5):1721-1730
56. Park SY, Zacharias C, Harrison C, Fan RE, Kunder C, Hatami N, Giesel F, Ghanouni P, Daniel B, Loening AM, Sonn GA, Iagaru A. Gallium ⁶⁸ PSMA-11 PET/MR Imaging in Patients with Intermediate- or High-Risk Prostate Cancer. *Radiology*. 2018 Aug;288(2):495-505
57. Laudicella R, Rüschoff JH, Ferraro DA, Brada MD, Hausmann D, Mebert I, Maurer A, Hermanns T, Eberli D, Rupp NJ, Burger IA. Infiltrative growth pattern of prostate cancer is

associated with lower uptake on PSMA PET and reduced diffusion restriction on mpMRI. Eur J Nucl Med Mol Imaging. 2022 Sep;49(11):3917-3928

58. Fedorov A, Beichel R, Kalpathy-Cramer J, Finet J, Fillion-Robin JC, Pujol S, Bauer C, Jennings D, Fennessy F, Sonka M, Buatti J, Aylward S, Miller JV, Pieper S, Kikinis R. 3D Slicer as an image computing platform for the Quantitative Imaging Network. Magn Reson Imaging. 2012 Nov;30(9):1323-41